**Pengtao Yue · Shernita Lee · Shahriar Afkhami ·
Yuriko Renardy**

On the motion of superparamagnetic particles in magnetic drug targeting

Abstract A stochastic ODE model is developed for the motion of a superparamagnetic cluster suspended in a Hagen-Poiseuille flow and guided by an external magnet to travel to a target. The specific application is magnetic drug targeting, with clusters in the range of 10–200 nm radii. As a first approximation, we use a magnetic dipole model for the external magnet and focus on a venule of 10^{-4} m radius close to the surface of the skin as the pathway for the clusters. The time of arrival at the target is calculated numerically. Variations in release position, background flow, magnetic field strength, number of clusters, and stochastic effects are assessed. The capture rate is found to depend weakly on variations in the velocity profile, and strongly on the cluster size, the magnetic moment, and the distance between the magnet and the blood vessel wall. A useful condition is derived for the optimal capture rate. The case of simultaneous release of many clusters is investigated. Their accumulation in a neighborhood of the target at the venule wall follows a normal distribution with the standard deviation roughly half of the distance between the magnet and the target. Ideally, this deviation should equal the tumor radius, and the magnet should be beneath the center of the tumor. The optimal injection site for a cluster is found to be just prior to arrival at the target. Two separate mechanisms for capturing a cluster are the magnetic force and, for radii smaller than 20 nm, Brownian motion. For the latter case, the capture rate is enhanced by Brownian motion when the cluster is released near the wall.

1 Introduction

Magnetic drug targeting is a method of delivering drugs to targets within the body by loading magnetic nanoparticles with therapeutic drugs, delivering them into the bloodstream, and guiding them with external magnets toward a tumor [1]. Recent reviews present the pros and cons of this highly localized treatment protocol [2–11]. Since the magnet is external, and the nanoparticles are attracted toward it, tumors closest to the magnet are more amenable to this form of targeting. Tumors that are located close to the surface, say less than 20 mm deep, are the best candidates [12] and this is the range in our study. In the larger arteries and veins, the field must counteract the fast blood flow, which drags the nanoparticles away from the target. Thus, the arterioles and venules with lower velocities improve the probability of targeting. With respect to the penetration of magnetic fields into the body, the article of [12] itemizes the methodologies that may be used to enhance and

P. Yue · Y. Renardy (✉)
Department of Mathematics, Virginia Tech, 460 McBryde Hall, Blacksburg, VA 24061-0123, USA
E-mail: renardy@vt.edu

S. Lee
Interdisciplinary Program for Genetics, Bioinformatics and Computational Biology,
Virginia Tech, Blacksburg, VA 24061, USA

S. Afkhami
Department of Mathematical Sciences, New Jersey Institute of Technology, Newark, NJ 07102, USA

stabilize magnetic levitation. Superconductors have been used in [13] to generate magnetic field gradients of 20–50 Tm^{-1} at a distance of 20 mm, for instance. Particles of mean size 100 nm and mass saturation magnetization of 81.7 Am^2 Kg^{-1} were injected into blood flow with velocity 100 mm s^{-1} in a tube of diameter 2 mm. The particles accumulated at the target site, showing promise of future developments for depositing particles against higher blood flow velocities and deeper within the body.

The main advantage of using magnetizable particles is that the treatment is localized, because the drugs are bound to the nanoparticles which are injected into the blood stream close to the tumor. This reduces overall side effects, compared with chemotherapy which is a systemic treatment that delivers chemicals to parts of the body which do not require them. A second advantage is that by adjusting the applied magnetic field, a high concentration of the particles can be attracted to a specific target site and kept there. Recent technologies that enable cluster designs to be smaller and of more uniform size for potential use in magnetic targeting have prompted renewed efforts to understand the motion of a cluster in blood vessels. This is the motivation for this study. A cluster of superparamagnetic nanoparticles can carry more load than individual particles, and furthermore, the advantage of superparamagnetism over a magnetized material is that the particles become magnetized only in the presence of a magnetic field. Superparamagnetic particles have the property that their dipoles are randomly oriented until a magnetic field is turned on [14]. Unlike a ferromagnet that exhibits spontaneous alignment of dipoles in the absence of an external magnetic field, the superparamagnetic particles are magnetized in random directions, and the poles keep flipping on a fast timescale known as the Néel relaxation time. Because they are small, the energy for the flipping comes from thermal energy. When a magnet is turned on in the presence of a superparamagnetic particle, the particle aligns to the poles and stays that way. When the magnet is switched to a different alignment, then the material responds to that on a timescale known as a magnetic relaxation time. Both of these relaxation timescales are small compared with the transit times that we model in this paper. When the drug targeting is finished, the magnetic field is turned off, and the superparamagnetic material does not retain any magnetization. The minimization of particle size is also important for evading the body's reticulo-endothelial system. In particular, a class of superparamagnetic nanoparticles having a size less than 10 nm have been recognized for their '*high magnetic saturation, negligible toxicity, and easier surface modifications*' [15].

Superconductors have been shown to generate magnetic field gradients of 20–50 Tm^{-1} at a distance of 20 mm, which is considerably higher than can be achieved by a permanent magnet [13]. Deeper targets will require technological advances in magnetic levitation. Since our study focusses on near-surface targets, we model flow conditions in venules of the order of 10^{-4} m. In comparison with the larger arteries and veins, the flow is slower. We begin with Newtonian pressure-driven flow, which is the simplest model for blood flow, followed by an assessment of the influence of velocity profiles induced by changes in the properties of the fluid.

The specific clusters modeled in this paper are chemically characterized in [16–20] and are composed of nanoparticles with a mean diameter of as low as 3 to 4 nm coated with oleic acid, a biocompatible polymer. The synthesis of stable clusters with controlled diameters ranging from 10 to 200 nm and containing a specified number of nanoparticles is described in [21]. Each cluster is approximately spherical [21–23]. We therefore investigate clusters with radii of order 10–100 nm. Brownian motion affects the dynamics if thermal energy is much larger than the magnetic energy. This well-known estimate leads to the diameter being smaller than $(6kT/\pi\mu_0 MH)^{1/3}$ [14]. The calculations presented in this paper therefore include Brownian effects for the smallest clusters.

Section 2 presents a simplified model for the time-dependent trajectory of a cluster released into blood flow. The importance of the sinusoidal component of pumping is assessed and found to be weak for a small blood vessel such as the venule. The cluster is modeled as an undeformable sphere in a flow regime where inertia is not important. Thus, the Stokes drag for a solid sphere is incorporated. The 'target' is located at a prescribed position on the tube wall, and a prescribed magnetic field is applied by an external magnet. Since our cluster is superparamagnetic, it moves in response to the applied magnetic field. A set of coupled ordinary differential equations which model the motion of the spherical particle in a tube filled with a viscous liquid is developed. The aim is to track the cluster as a function of initial position, flow parameters and magnetic parameters. This approach is similar to the models developed in [24–26]. A difference is that we track the transient motion of single clusters rather than use a continuum approximation, for instance, an advection-diffusion model for the concentration of particles [12,27]. In [28], the magnetic force is assumed to be a constant, which is a simplifying assumption not made in this paper, but should be applicable if the size of the blood vessel is sufficiently small compared with the distance from the magnet. Initially, the particle density is a constant across the blood vessel. They find three main regimes of behavior: (i) magnetic force dominated, (ii) velocity dominated, and

(iii) boundary layer formation where magnetic and drag forces are comparable. The latter is an interesting case where the density of the nanoparticles can rise in the endothelial layer which consists of membranous cells between the blood vessel and surrounding tissue. These qualitative regimes also appear in our results, if the cluster (i) lies in the direction of the magnetic field vector in a low velocity region, (ii) is at the centerline where the blood velocity is highest and provided the magnetic field is relatively weak, and (iii) the cluster arrives at a wall upstream of the target and slides slowly to the target, resulting in the possibility of attraction toward the magnet through a membranous wall. Numerical studies which address specific conditions in larger arteries and veins, such as the effects of inertia, pressure oscillations, and bifurcations in channel shapes, may also be of interest to the reader [29,30]. Experimental data on the correlation between magnetic forces and blood velocities required to capture nanoparticles flowing through an array of microcapillaries are given in [31]. This study finds that the particles are captured in locations that vary in magnetic field strength, and the locations were strongly influenced by the flow rate through the array. A Neodymium Iron Boron (NdFeB) block magnet is used, and strategies are suggested for future designs of magnetic shapes. The use of a general software package for magnetic drug targeting in 2D is depicted in [32], although the limitations of the approach are not clearly stated. The model equations are found in [33] which contains errors. There is a clear need for further experimental, numerical, and mathematical studies to investigate the feasibility of biomedical applications.

2 Governing equations

Figure 1 is a schematic of our mathematical model. The blood vessel is modeled by a cylindrical tube of radius R, with its axis along the x-axis. The tumor is modeled by a target located at the wall at $x = 0$, $y = 0$, $z = -R$. The imposed flow is Hagen-Poiseuille flow with a non-zero velocity component in the x-direction, $(u(y, z, t), 0, 0)$, satisfying no-slip conditions at the walls $y^2 + z^2 = R^2$. The blood vessel is on the scale of a venule (radius $R = 10^{-4}$ m), which is small enough that the pressure oscillations due to cardiac pulsing is found to be low, and Stokes flow is an appropriate approximation. The fluid equation of motion is the Stokes equation, $0 = -\frac{\partial p}{\partial x} + \eta \Delta u$, where η is the viscosity of the liquid. A pressure gradient is imposed resulting in

$$u = [u_{\max} + u_{\mathrm{osc}} \cos(\omega t)] \left(1 - \frac{y^2 + z^2}{R^2}\right), \tag{1}$$

where $u_{\max}$, u_{osc}, R, and ω are prescribed. For our parameter range, we shall see that u_{osc} has a weak effect. This flow field generates a Stokes drag force for a rigid sphere:

$$\mathbf{F}_v = -D\mathbf{v}_s, \quad D = 6\pi \eta a, \quad \mathbf{v}_s = \frac{d\mathbf{x}}{dt} - \mathbf{u_b}, \tag{2}$$

where $\mathbf{v}_s$ is the velocity of the particle relative to the surrounding liquid, namely the slip velocity. Here, $\mathbf{u_b} = (u, 0, 0)$ where u is determined by (1), $\mathbf{x}(t) = (x(t), y(t), z(t))$ is the location of the cluster, and D is the friction coefficient.

The external magnetic field in the absence of the cluster is denoted by $\mathbf{H}_e$, following the notation of [14,35–37]. The magnetic induction is $\mathbf{B} = \mu \mathbf{H}$, where the permeability is $\mu = \mu_0(1 + \chi)$, the permeability of vacuum is $\mu_0 = 4\pi \times 10^{-7}$ N A^{-2}, and the susceptibility is χ. For simplicity, χ is assumed to be a constant, but this actually depends on the magnetic field strength. The constant approximation holds for low fields, up to about 20 kA m^{-1}. However, as the field gets larger the susceptibility is no longer linear, and the effective susceptibility reduces. This reduces the magnetic force on the particles at larger applied fields. A comparison of the constant versus variable susceptibility on the capture rate is evaluated at the end of Sect. 3.3.3.

Maxwell's equations are curl $\mathbf{H}_e = \mathbf{0}$ and div $\mathbf{H}_e = 0$. Thus, $\mathbf{H}_e = \nabla \phi$, where ϕ is a harmonic function. We can then rewrite

$$(\mathbf{H}_e \cdot \nabla)\mathbf{H}_e = \frac{1}{2}\nabla(|\nabla\phi|^2), \tag{3}$$

where ϕ can be calculated when the external magnetic field data are prescribed.

The magnet is modeled by a magnetic dipole. We shall see that the most effective position for it is directly beneath the target. However, there is typically some distance between the blood vessel and the skin where the
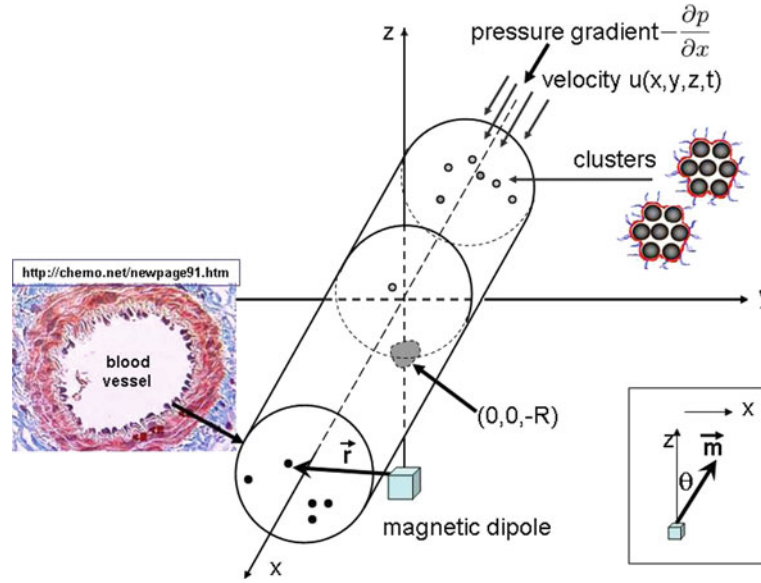
Fig. 1 Schematic of mathematical model for clusters guided toward a target at $(0, 0, -R)$ in a cylindrical blood vessel of radius R by an applied magnetic field. The magnetic point dipole (4) models the external magnet of strength $|\mathbf{m}|$, with vector $\mathbf{r}$ pointing from the magnet to the cluster. The dipole moment vector $\mathbf{m}$ points from the magnet placed below the target, and points at an angle θ to the positive x-axis. With this definition, $\theta = 0$ is a vector pointing directly upward. The cross-sectional slide is from http://chemo.net/newpage91.htm [34]

magnet is placed. The dipole moment is denoted by $\mathbf{m}$, where its direction and magnitude are prescribed and fixed, as sketched in Fig. 1. The external magnetic field potential is the well-known equation [14],

$$\phi = -\frac{1}{4\pi} \frac{\mathbf{m} \cdot \mathbf{r}}{r^3}, \tag{4}$$

where $\mathbf{r}$ is the vector pointing from the dipole to the superparamagnetic cluster, and $|\mathbf{r}| = r$. This gives the magnetic field,

$$\mathbf{H}_e = \nabla\phi = -\frac{1}{4\pi} \frac{\mathbf{m}}{r^3} + \frac{3}{4\pi} \frac{\mathbf{m} \cdot \mathbf{r}}{r^4} \frac{\mathbf{r}}{r}. \tag{5}$$

The force on the magnetic body in an external field is, in general, given by

$$\mathbf{F}_m = \int_V \mu_0 (\mathbf{M} \cdot \nabla) \mathbf{H}_e \, dV. \tag{6}$$

The magnetization is $\mathbf{M} = \chi\mathbf{H}$, where $\mathbf{H}$ now denotes the actual field, which has been modified by the presence of the body. For a small particle, we can assume that the external field is approximately constant on the scale of the particle, and we can replace $\mathbf{M}$ by the magnetization induced in a uniform external field. For a spherical particle, this yields the Clausius-Mossotti formula [38,39], and the magnetization inside the sphere is uniform, with magnitude

$$\mathbf{M} = \frac{3\chi}{3 + \chi} \mathbf{H}_e. \tag{7}$$

Hence, the force (6) is

$$\mathbf{F}_m = V \frac{3\mu_0 \chi}{3 + \chi} (\mathbf{H}_e \cdot \nabla) \mathbf{H}_e, \tag{8}$$

where $V = \frac{4}{3}\pi a^3$ is the volume of the cluster, a is the radius of the cluster, and $\mathbf{H}_e$ is the given external magnetic field.

The relaxation time for magnetization of the nanoparticles is of order 10^{-7} s at $T = 25°C$, and we shall assume here that the time taken for magnetization is instantaneous. The motion of the cluster is therefore given by the balance

$$\mathbf{F}_m + \mathbf{F}_v = 0. \tag{9}$$

This leads to the following ordinary differential equations:

$$\frac{d\mathbf{x}}{dt} = \mathbf{u_b} + 2c(\mathbf{H}_e \cdot \nabla)\mathbf{H}_e, \quad c = \frac{\mu_0 \chi a^2}{3(3 + \chi)\eta} \tag{10}$$

or

$$\frac{dx}{dt} = u(y, z, t) + c\frac{\partial}{\partial x}(|\nabla\phi|^2), \tag{11}$$

$$\frac{dy}{dt} = c\frac{\partial}{\partial y}(|\nabla\phi(x, y, z)|^2), \tag{12}$$

$$\frac{dz}{dt} = c\frac{\partial}{\partial z}(|\nabla\phi(x, y, z)|^2). \tag{13}$$

In the absence of Brownian motion, the initial value problem is integrated numerically [40].

Brownian motion is intrinsically three dimensional and only relevant for the smallest clusters. When we do incorporate Langevin's Brownian motion model [14,41], the governing equation changes because of the stochastic forcing vector

$$\frac{\sqrt{2DkT}}{\sqrt{dt}}(\mathbf{N}(0, 1)) = \frac{\sqrt{2DkT}}{\sqrt{dt}}(N_1(0, 1), N_2(0, 1), N_3(0, 1)). \tag{14}$$

Here, $N_1(0, 1)$, $N_2(0, 1)$, and $N_3(0, 1)$ denote independently generated, normally distributed, random variables with zero mean and unit variance [42]. k is Boltzmann's constant 1.38×10^{-23} N m K^{-1}, and T is the absolute temperature in degrees Kelvin. The random variables $N_i(0, 1)$, $i = 1, 2, 3$, are constants over very short time intervals dt and change randomly with a Gaussian distribution. The average magnitude of the distribution for the stochastic forcing vector is zero. The variance, defined as the average of the square of the force, is $2DkT/dt$. In place of (11)–(13), we have

$$\rho V\frac{d^2\mathbf{x}}{dt^2} = -D\left(\frac{d\mathbf{x}}{dt} - \mathbf{u_b}\right) + \frac{3\chi V\mu_0}{3 + \chi}\nabla\left(\frac{1}{2}|\nabla\phi|^2\right) + \frac{\sqrt{2DkT}}{\sqrt{dt}}\mathbf{N}(0, 1), \tag{15}$$

where ρ is the density of the cluster, and $\mathbf{u_b}$ is the base flow. We estimate that the inertia, or acceleration, term on the left hand side is important for only a short interval of time compared with the dynamics described by the remaining terms. This timescale for the inertia versus the viscous term is $\frac{\rho V}{D} = \frac{2\rho a^2}{9\eta}$. In the range of cluster sizes for which we conduct the numerical integration of (15) in Sect. 3.4, this timescale is negligible; hence, inertia is neglected.

The system (15) is expressed in the following general format:

$$dX_t = f(X_t)dt + g\,dW_t, \tag{16}$$

where X_t is an $n \times 1$ state vector of process variables, $f(X_t)$ is an $n \times 1$ drift-rate vector, g is an $n \times n$ instantaneous diffusion-rate matrix, and dW_t is an $n \times 1$ vector of non-correlated random numbers $\sqrt{dt}\,N(0, 1)$. In particular, X_t, $f(X_t)$ and g are:

$$X_t = \mathbf{x}^T = (x(t), y(t), z(t))^T, \tag{17}$$

$$f(X_t) = \left[\mathbf{u_b}(\mathbf{x}, t) + \frac{3\chi V\mu_0}{(3 + \chi)D}\nabla\left(\frac{1}{2}|\nabla\phi(\mathbf{x})|^2\right)\right]^T, \tag{18}$$

$$g = \sqrt{\frac{2kT}{D}}\mathbf{I}, \tag{19}$$

where $\mathbf{I}$ is the 3×3 identity matrix. The system (16) of stochastic ordinary differential equations is integrated using [43], which implements the Euler-Maruyama method.

3 Numerical results

3.1 Motion of a cluster in the absence of background flow

We begin by examining the limiting case of small or zero background flow; the cluster is initially placed at $\mathbf{r}_0$ and is pulled toward the magnet through a quiescent liquid. In this case, we can formulate analytical estimates for the transit time. When the time taken to arrive at the target is investigated by varying the angle subtended by the magnetic dipole, we find that the travel time is minimized when $\mathbf{m} \parallel \mathbf{r}_0$. This means that when the cluster is positioned directly in the path of the dipole moment vector, it is attracted to the magnet in the fastest time possible. Moreover, the cluster approaches the magnet along a straight line, and we can denote the distance of the cluster from the magnet to be a scalar variable $r(t)$. Therefore the magnetic force (8) simplifies to

$$f_m = -\left(\frac{3\chi}{3+\chi}\right)\left(\frac{\mu_0}{\pi}\right)\left(\frac{m^2 a^3}{r^7}\right), \quad m = |\mathbf{m}|, \ r = |\mathbf{r}|, \tag{20}$$

and the viscous drag is

$$f_v = -6\pi \eta a \frac{dr}{dt}. \tag{21}$$

The negative sign here means that the direction of the viscous force is toward the dipole. The force balance (9) yields an ordinary differential equation for $r(t)$. Integration from the initial distance $r = r_0$, where $r_0 = |\mathbf{r}_0|$, to the magnet at $r = 0$ yields the minimal transit (or travel) time:

$$t_{\min} = \frac{3\pi^2}{4\mu_0}\left(\frac{3+\chi}{3\chi}\right) a^{-2} m^{-2} \eta r_0^8. \tag{22}$$

This equation is useful since it shows explicitly the dependence of the minimal transit time on χ, a, m, η, and r_0.

A Newtonian fluid with three to four times the viscosity of water is used as a model of blood in an artery or vein. This is a typical range although there are diseases that increase the viscosity to much higher values. Therefore, we let $\rho = 10^3$ Kg m^{-3}, $R = 10^{-7}$ m, and $\eta = 4 \times 10^{-3}$ Pa s. Figure 3 of [44] shows experimentally measured magnetic field magnitudes $|\mathbf{H}|$ as functions of distance from a typical magnet; from this, we use a distance 0.005 m and $|\mathbf{H}| = 18{,}000$ Am^{-1}.

For the case $\mathbf{m} \parallel \mathbf{r}$, Eq. (5) simplifies and yields $|\mathbf{H}| = \frac{1}{2\pi r^3}m$. This leads to an estimate for the magnetic dipole moment of $m = 0.01$ A m^2. We take $\chi = 0.2$ as in the nanoparticle sample of [35] and $a = 10^{-7}$ m. For the initial distance $r_0 = 10^{-4}$ m which is of the order of the vessel size R, Eq. (22) yields the minimal transit time $t_{\min} = 1.26 \times 10^{-9}$ s. The transit time increases with r_0 so that at a larger initial distance we have $t_{\min} = 0.13$ s for $r_0 = 10^{-3}$ m.

A second instance where the cluster moves along a straight line is $\mathbf{m} \perp \mathbf{r}_0$. The magnetic force is a quarter of the f_m in Eq. (20). We verify that this corresponds to the maximal transit time $t_{\max} = 4t_{\min}$. The transit time as a function of the magnetic dipole orientation is shown in Fig. 2 for the case where the particle is initially placed above the target. Since the particle is on the z-axis, above the target and the magnet, this is a simplest case scenario for evaluating the dependence of the time taken by the cluster to reach the target when the magnetic field direction is varied from the negative x-axis (downstream, $-90° < \theta < 0$) to the positive x-axis (upstream, $0 < \theta < 90°$) along the cylindrical axis. Clearly, when the magnetic field points vertically upwards, right at the cluster, the transit time is shortest. Since there is no background flow, the result for the magnetic field pointing upstream $-90° \leq \theta \leq 0$ is symmetric across $\theta = 0$ to the results in Fig. 2.

3.2 Effect of blood flow on cluster motion

The strength of the background pulsating base flow (1) is important for large arteries and less so for small veins which are typically found closer to the skin surface. Here, we shall conduct our investigation with reference to the orders of magnitudes for venules of the skeletal muscle in cats [45]. First, if the flow is simplified by the
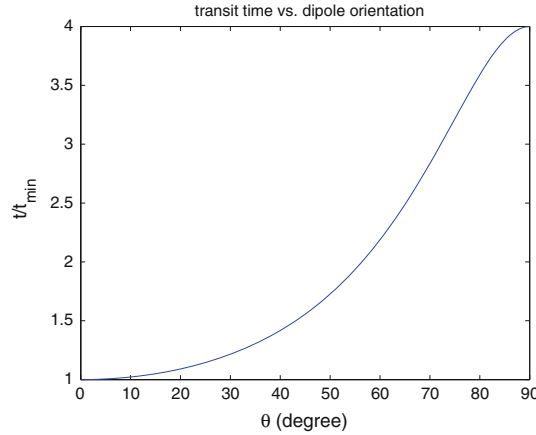
Fig. 2 Transit time versus magnetic field orientation θ measured from the vertical axis with no background flow. The particle is initially above the magnet. $0 < \theta < 90°$ corresponds to the magnetic field pointing *downstream*. The physical problem has inherent symmetry across the vertical axis at $\theta = 0$ to negative values (pointing *upstream*). The minimum transit time follows the analytical formula Eq. (22)

absence of pulsations, then $u = u_{\max}(1 - \frac{r^2}{R^2})$. This gives the flow rate

$$\int_0^R 2\pi r u \mathrm{d}r = \frac{\pi}{2} u_{\max} R^2, \tag{23}$$

which we estimate to be of the order of 10^{-10} m^3 s^{-1} based on [45]. With $R = 10^{-4}$ m, we find $u_{\max} = \frac{2}{\pi} \times 10^{-2}$ m s^{-1}, which also agrees with the magnitude of the recorded dual-slit velocity in [45]. If the flow were in a larger blood vessel, then we would use the systolic and diastolic blood pressure data of 120–80 mm Hg, respectively, and estimate the parameters in our base flow; $\frac{u_{\max} + u_{\mathrm{osc}}}{u_{\max} - u_{\mathrm{osc}}} = \frac{120}{80}$, which yields $u_{\mathrm{osc}} = \frac{u_{\max}}{5}$. A pulse of 180 beats per minute gives the period $\frac{2\pi}{\omega} = \frac{60}{180} = 0.3$ s, or $\omega = 18$ s^{-1}. For venules, the time-periodic component of the base flow is negligible with respect to the unidirectional component, so that without the basic unidirectional background flow, there is essentially no flow. Hence, a cluster placed above the magnet travels toward it at the times shown in Fig. 2.

The effect of blood flow (1) on the transit time is shown in Fig. 3. This figure shows the angle θ subtended by the magnetic moment vector (cf. Fig. 1) versus time taken for the cluster to arrive at the target. The cylindrical radius is again $R = 10^{-4}$ m, $u_{\max}$ in (1) is $\frac{2}{\pi} \times 10^{-2}$ m s^{-1}, $u_{\mathrm{osc}} = \frac{u_{\max}}{5}$, $\omega = 18$ s^{-1}, $a = 10^{-7}$ m, $\eta = 0.004$ Pa s, and $\chi = 0.2$. The cluster is released at $(-10^{-3}$ m, 0, 0). This is *upstream* of the target and the dipole which are located at the bottom wall $(0, 0, -R)$. The cluster would be carried by the flow, starting along the cylindrical axis, and influenced by the magnetic field. If it passes over the magnet, and goes *downstream* in the positive x-direction, the cluster misses the target. The figure shows the minimum transit time at roughly -83 to $-82°$. Note that when there is no flow, the moment vector should point directly at the released cluster, so that a right angle triangle with vertical height to horizontal base length in the ratio -1 to 10 defines the magnetic field vector (the hypotenuse). Thus, $\tan \theta = -10$, which yields $\theta = -84°$. Figure 3 shows the effect of the flow in moving the cluster toward the positive x-axis, giving a smaller optimal magnitude $|\theta|$.

A sufficient condition for the cluster to hit the target is estimated as follows. Since the flow is parallel flow, the initial placement of the cluster at a point downstream of the target ($\mathbf{r_0} \perp \mathbf{m}$ and $\mathbf{r_0} \parallel \mathbf{u}$) would ensure that it would avoid the target. The cluster hits the target if the magnetic force ($f_m/4$ in Eq. (20)) wins over the Stokes drag (see Eq. (21)), which leads to an over-conservative sufficient condition

$$\frac{u r_0^7}{m^2 a^2} < C, \quad C = \frac{\mu_0}{24\pi^2 \eta} \frac{3\chi}{3 + \chi}. \tag{24}$$

For a conservative estimate, we may let u represent the maximum velocity and r_0 be the radius of the venule. For the above blood flow, $u = \frac{2}{\pi} \times 10^{-2}$ m s^{-1} and $r_0 = 10^{-4}$ m lead to $m > 1.6 \times 10^{-5}$ A m^2. This result is confirmed by the numerical simulation shown in Fig. 4. For a model of flow through a venule, the oscillatory
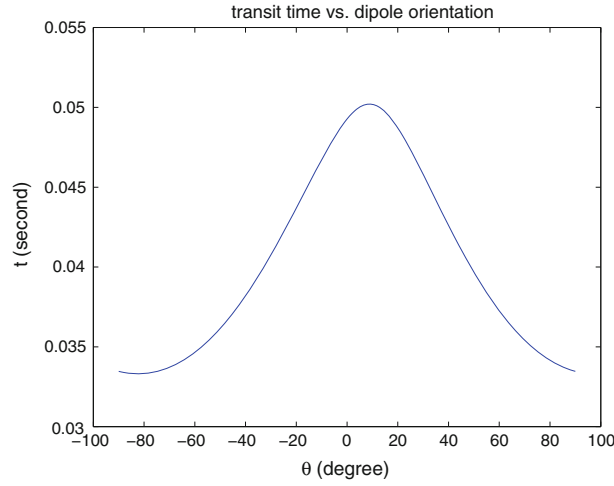
Fig. 3 The time taken for a cluster released at $(-10^{-3}$ m, 0, 0) as a function of moment vector angle θ. The background flow is u given by (1), where $u_{\max} = \frac{2}{\pi} \times 10^{-2}$ m s^{-1} and $u_{\mathrm{osc}} = \frac{u_{\max}}{5}$, $\omega = 18$ s^{-1}. The venule radius is $R = 10^{-4}$ m, the cluster radius is $a = 10^{-7}$ m, the viscosity $\eta = 0.004$ Pa s, and susceptibility $\chi = 0.2$. The dipole is located at $(0, 0, -R)$. The minimum transit time occurs when $\theta = -83°$

component is known to be insignificant compared with the rest of the base flow. Therefore, we let $u_{\mathrm{osc}} = 0$ in (1)) for the simulations in Fig. 4. The initial position of the cluster is far upstream of the target at $(-10R, 0, 0)$ on the centerline axis of the blood vessel. The target and the dipole are at the vessel wall at $(0, 0, -R)$. This placement of the dipole, while theoretically optimal, is a first approximation to a proximal exterior location. The figure shows the magnetic dipole moment m versus the moment vector angle θ, which are two controllable and inputted properties of the magnet. The regime above the curve is the desirable operational regime for magnetic drug targeting. When a cluster is in that area, it hits the target, but below the delineating curve, the cluster misses the target. In each numerical simulation, a cluster travels some distance from release and is attracted by the magnetic field, so that it moves away from the cylindrical axis toward the lower wall. Here, the speed is not as high as it is at the centerline, so that the cluster is captured with less m when $\theta = 0$ as when it was released at $\theta = -83°$. This is one reason for the critical curve for hit-or-miss to dip down at $\theta = 0$. In addition, we probe the sensitivity of this curve to changes in the base flow. The data points $\square$ represent results for a viscoplastic flow with most of the velocity profile being plug flow: $v = v_{\max}$, e.g., $v = v_{\max}[1 - (\frac{r}{R})^n]$, $n \gg 2$. Therefore, the figure shows negligible effect on the position of the hit-or-miss curve even when the base flow changes to a shear-thinning power-law flow. This is important because flows in circulation may not be simply parabolic; due to the rheological influence of the red blood cells [46], power-law base flows have been used to model blood flow [47]. We have shown here that the results are not sensitive to the flow profile, but strongly depend on the dipole moment and maximum velocity.

We next delve further to understand the results of Fig. 4. When the cluster approaches the target, the base flow decreases in magnitude toward the vessel wall while the magnetic field increases. This is clear from examining the slip velocity $\mathbf{u}_m$, which is due to the magnetic force, and is the second term on the right hand side of (10):

$$\mathbf{u}_m = \frac{3\chi}{3 + \chi} \frac{V\mu_0}{D} \nabla \left(\frac{1}{2} |\nabla \phi|^2 \right).$$

We see the dependence on r^{-7} as $r \to 0$. Therefore, $\mathbf{u_m} \sim \mathbf{u_b}$ at a critical distance $r = r_c$,

$$r_c = \left(\frac{Cm^2 a^2}{u} \right)^{1/7}. \tag{25}$$

For distances less than the critical distance, the transit time is dominated by the magnetic force, and the base flow is negligible.
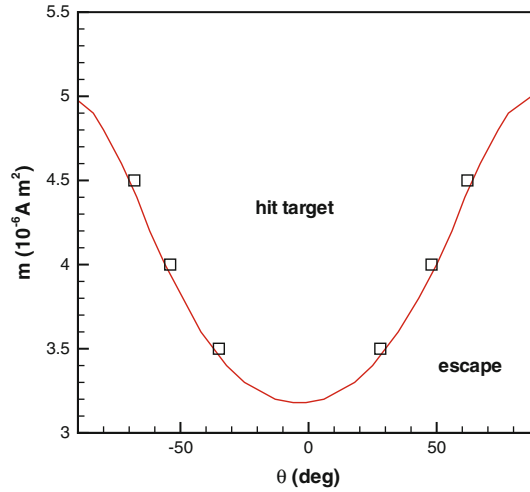
Fig. 4 Whether a cluster hits a target or misses it is delineated by the curve shown in this figure. The magnetic moment m and the angle θ (cf. Fig. 1) are inputted properties of a magnet. The cluster is released at $(-10R, 0, 0)$ far upstream of the target at $(0, 0, -R)$. The dipole is located at the target. Above the curve, the cluster hits the target. The background flow (1) is steady ($u_{osc} = 0$): $R = 10^{-4}$ m, $u_{max} = \frac{2}{\pi} \times 10^{-2}$ m s^{-1}, $a = 10^{-7}$ m, $\eta = 0.004$ Pa s, and $\chi = 0.2$. The data points *open square* are for the power-law base flow relevant to blood flow; these lie on *top* of the curve for the Hagen-Poiseuille flow

Table 1 Transit time for different magnetic dipole moments m

m (A m^2)	t (s) (numerical)	t_{min} (s) (Eq. 22)	r_c (m) (Eq. 25)
10^{-2}	1.26×10^{-9}	1.26×10^{-9}	6.29×10^{-4}
10^{-4}	1.26×10^{-5}	1.26×10^{-5}	1.69×10^{-4}
10^{-5}	1.27×10^{-3}	1.26×10^{-3}	8.74×10^{-5}
5×10^{-6}	6.53×10^{-3}	5.03×10^{-3}	7.17×10^{-5}
4.5×10^{-6}	1.23×10^{-2}	6.21×10^{-3}	6.96×10^{-5}
4.4×10^{-6}	∞	6.49×10^{-3}	6.92×10^{-5}

Base flow (1) is $u = u_{max}(1 - \frac{y^2+z^2}{R^2})$, $R = 10^{-4}$ m, $u_{max} = \frac{2}{\pi} \times 10^{-2}$ m s^{-1}, $a = 10^{-7}$ m, $\eta = 0.004$ Pa s, and $\chi = 0.2$. The cluster is initially at $(0, 0, 0)$, directly above the magnet

An alternative way to explain why the base flow can be neglected if r is smaller than r_c is based on recalling the transit time in a liquid at rest (22). In this case, (24) is equivalent to

$$u t_{min} < \frac{1}{32} r_0. \tag{26}$$

This means that if the cluster is released at a distance r_0 right above the target, the displacement downstream is almost negligible during the travel time, and therefore, the influence of the base flow is also negligible.

A comparison between the transit times obtained by numerical computation of (10) and the formula (22) which neglects the base flow is provided in Table 1. For the given a, R, χ, η, and u, the critical magnetic dipole moment m_c lies between 4.4×10^{-6} and 4.5×10^{-6} A m^2. If m is increased by 10% above the critical value to 5×10^{-6} A m^2, then the transit time provided by Eq. (22) is evidently quite a good estimate. Note that the m_c here is higher than the one at $\theta = 0°$ in Fig. 4 because of the difference in initial conditions; the cluster in Fig. 4 is closer to the target when it passes over the target. A comparison of the third to the fifth rows of Table 1 shows that Eq. (25) underpredicts r_c, as the numerical simulations reveal the capture of clusters with initial distances $r_0 = R > r_c$. Overall, however, Eq. (25) serves as a useful estimate.

Hereafter, we shall focus on the following parameters unless otherwise indicated: $u = u_{max}(1 - \frac{y^2+z^2}{R^2})$, $R = 10^{-4}$ m, $u_{max} = \frac{2}{\pi} \times 10^{-2}$ m s^{-1}, $a = 10^{-7}$ m, $\eta = 0.004$ Pa s, and $\chi = 0.2$.
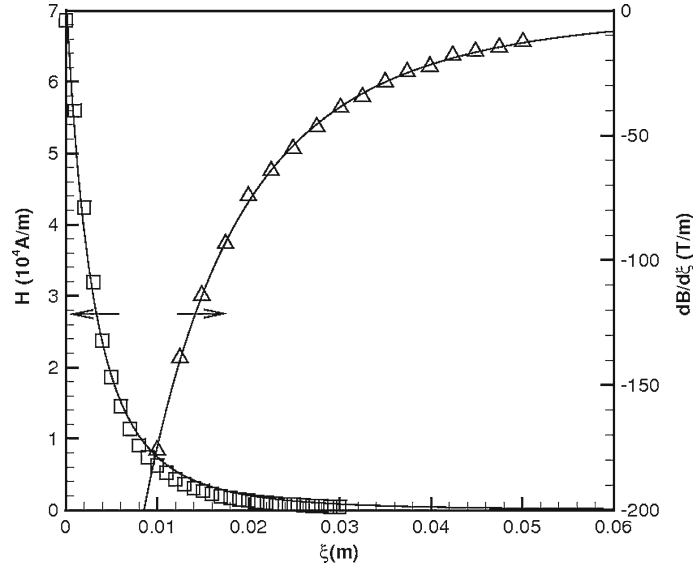
Fig. 5 Magnetic field strength H and gradient of magnetic induction $dB/d\xi$ along the dipole direction versus distance ξ from the magnet surface. Experimentally measured values for superconducting magnets in [44] (*open square*) and [13] (*open triangle*) compare well with (27) (*solid line*). These values are used for the numerical modeling in Sect. 3.3

3.3 Effect of separation distance between the magnetic dipole and the target

3.3.1 Simplified dipole model for experimentally obtained field data

In the previous section, the dipole is situated at the target on the vessel wall. However, this generates a magnetic field which yields a force singularity at the target which is unphysical. We ameliorate this in this section by situating the dipole at a suitable distance from the vessel wall, at $x = 0, y = 0, z = -R - d$. This models a magnet with its end situated at $z = -R$, and its center at a distance $d > 0$ vertically below the target. The magnetic field along the dipole direction is given by

$$H = \frac{1}{2\pi} \frac{m}{(\xi + d)^3},\tag{27}$$

where $(\xi + d)$ represents the distance vertically upwards from the center of mass of the magnet. An important question is whether the dipole is suitable for representing the field of a superconducting magnet realistically. To answer this, we compare the dipole formula (27) with two different sets of experimental measurements along the moment vector direction in Fig. 5. One data set is given for the magnetic field strength, and therefore we compare our results with that quantity. The other measured data set is the magnetic induction gradient and therefore we simulate the gradient, and plot both curves on the same figure. Here, the lines are predictions of our Eq. (27) with $m = 0.3121$ A m^2 and $d = 8.823 \times 10^{-3}$ m (magnet in [44], □) and $m = 1,066$ A m^2 and $d = 3.372 \times 10^{-2}$ m (magnet in [13], △). These correspond to $B = 0.091$ T and $B = 5.561$ T, respectively, at the magnet surface. Figure 5 shows very good agreement, and therefore this theoretical approach has a high pay-off. Figure 6 illustrates the magnetic field generated around a magnet in contact with the vessel wall at $x = 0, y = 0$, and with the center of mass located a distance d below the wall.

3.3.2 Slip model versus no-slip model

We investigate the case where the dipole is placed just below the target, and both are at $x = 0$. The cluster is released at the tube center upstream of the magnet. For the magnet in [44] ($m = 0.3121$ A m^2 and $d = 8.823 \times 10^{-3}$ m), the cluster is always flushed away before reaching the target. This is understandable because the transit time predicted by Eq. (22) in the absence of flow, for traveling from $r = R + d$ (at the tube axis, right above the magnet) to $r = d$ is 446.9 s. Given such a long estimated transit time due solely to the pull of the magnet, the cluster would be carried more than 1 m in the presence of the background flow and be completely out of range. This is clearly seen in Fig. 7, where the cluster trajectory is almost unaffected by the
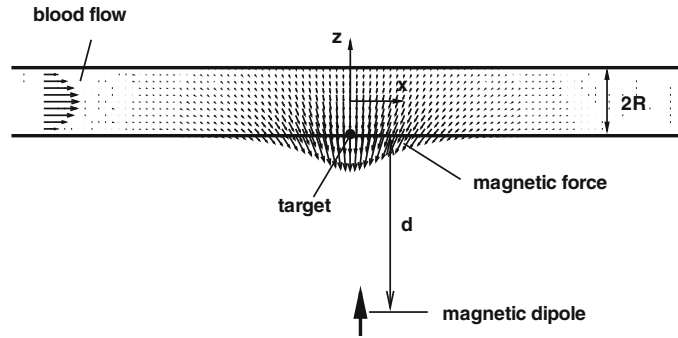
Fig. 6 Schematic of the vertical slice through the cylindrical vessel at $y = 0$. The magnetic force field is shown when the dipole is at a distance d below the vessel wall
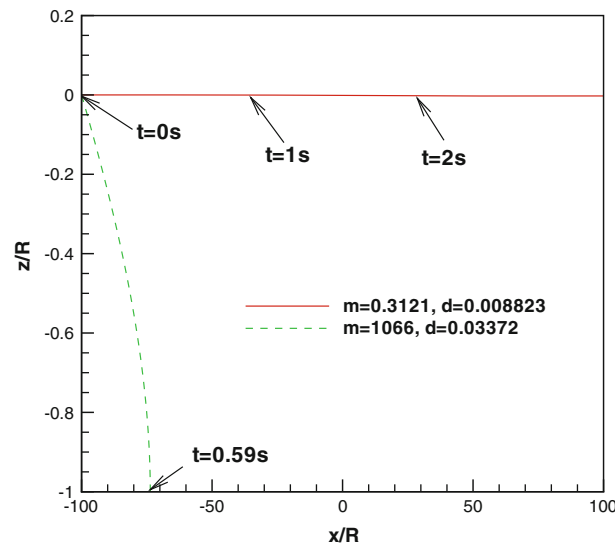

Fig. 7 Cluster trajectories. $R = 10^{-4}$ m, $u_{\max} = \frac{2}{\pi} \times 10^{-2}$ m s^{-1}, $a = 10^{-7}$ m, $\eta = 0.004$ Pa s, and $\chi = 0.2$. The magnetic dipole is placed at $(0, 0, -R - d)$ and the cluster is released from $(-100R, 0, 0)$

magnetic field. On the other hand, the magnet in [13] ($m = 1,066$ A m^2 and $d = 3.372 \times 10^{-2}$ m) is much stronger; the transit time estimated by Eq. (22) is 0.4 s. As a result, the background flow does not flush the cluster away before it is attracted to the magnet and hits the tube wall at $t = 0.59$ s. Moreover, Fig. 7 shows that the cluster impacts the wall at some distance away from the target point at $(0, 0, -R)$. This treatment is therefore potentially most useful for delivering drugs to a tumor that is located at the vessel wall. When the impact is within a certain range, say the tumor width, then it is a successful impact. In the following, we shall refer to the center of the tumor as the 'target'.

Up to this point, we have addressed the case of the cluster which is initially released along the central axis of the cylindrical vessel, where the base flow velocity is maximal. In the following, we allow the cluster to be released at a variety of positions in the circular cross-section of the vessel. A cluster that is initially closer to the wall would more likely be captured due to a lower convection velocity and a stronger field. When a cluster reaches the wall, the extreme cases are that it either slips along the wall or remains there. In the following, we study both models.

If the vessel wall is smooth or slippery, the clusters may slide after they hit the wall. Depending on the competition between the viscous drag and magnetic force, the cluster may slide toward or away from the target. To confine the clusters inside the vessel, we adopt a collision model similar to that in [48] by imposing an extra repulsion force if the cluster arrives too close to the vessel wall:

$$\mathbf{F_w} = \begin{cases} 0, & r + a < R - s, \\ \frac{A}{\epsilon_w} \left(\frac{R - r - a}{s} \right)^2 \mathbf{n}, & \text{otherwise.} \end{cases} \tag{28}$$
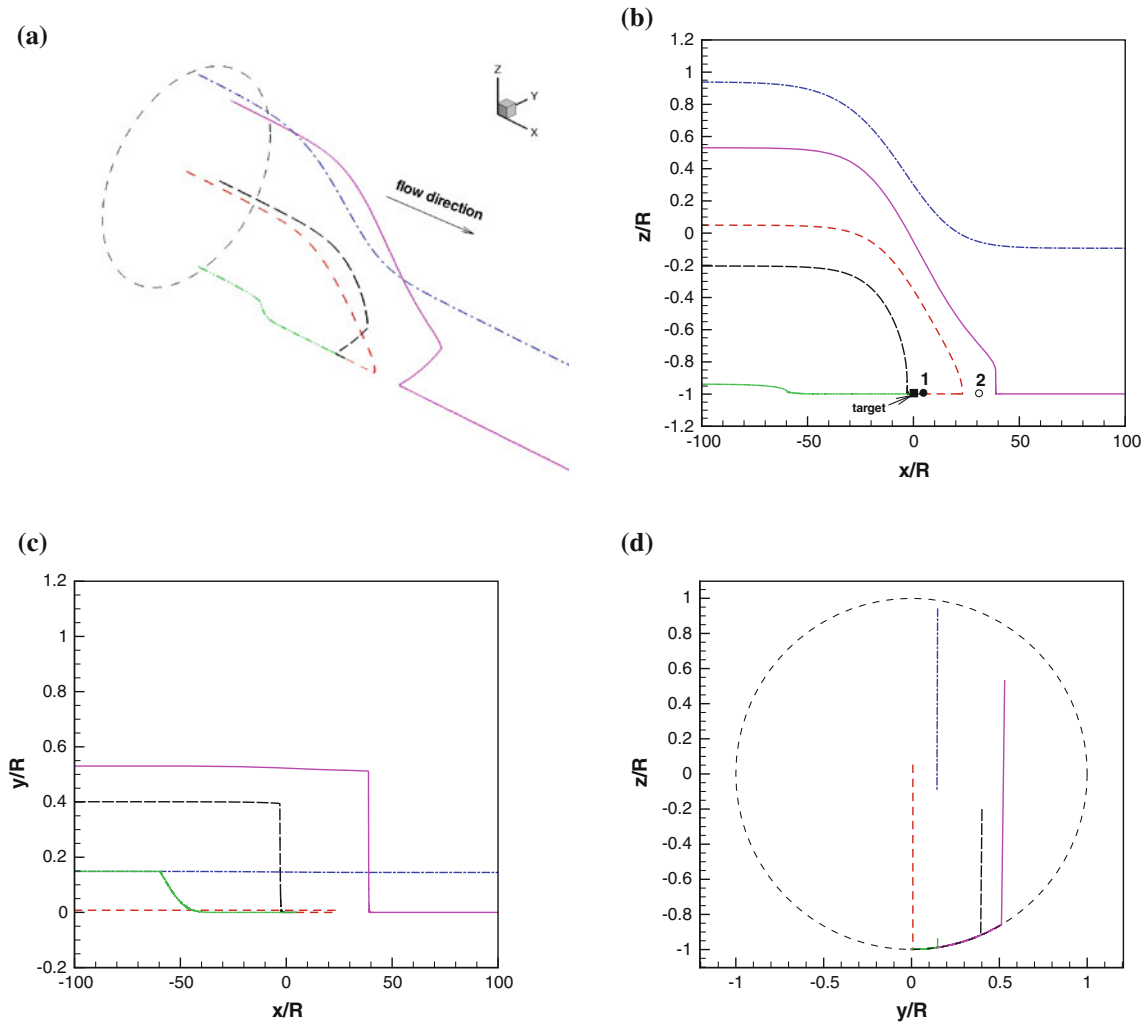
Fig. 8 Typical cluster trajectories with sliding motion on the wall. **a** shows the trajectories in three dimensions (compressed in the x-direction); **b**, **c** and **d** show the projection of trajectories on the $x - z$, $x - y$, and $y - z$ planes. $R = 10^{-4}$ m, $u_{max} = \frac{2}{\pi} \times 10^{-2}$ m s^{-1}, $a = 10^{-7}$ m, $\eta = 0.004$ Pa s, $\chi = 0.2$, $m = 1$ A m^2, and $d = 50R$. The clusters are released from $x = -100R$. In **b**, '1' denotes a stable equilibrium point and '2' denotes a saddle point

Here, $r = \sqrt{y^2 + z^2}$ where y and z are the coordinates of the cluster, **n** is the inward pointing unit normal to the vessel wall, s is the range of the repulsion force, A has the dimension of force, and ϵ_w is a small dimensionless number. In our calculations, we take $s = 0.1a$, $\epsilon_w = 0.1$, and $A = |\mathbf{F}_m \cdot \mathbf{n}|$ where $\mathbf{F}_m$ is the magnetic force on the cluster. This yields a system of stiff ordinary differential equations which we solve numerically [49].

Figure 8 illustrates the trajectories that represent different properties. The trajectories can be divided into three categories: trajectories that escape without hitting the vessel wall (e.g., the dash-dot trajectory), trajectories that escape after hitting the vessel wall (e.g., the solid trajectory), and trajectories that eventually get captured by the magnet (e.g., other trajectories). Along the bottom wall, there are typically two locations where the drag force is balanced by the x-component of the magnetic force: a stable equilibrium point (point 1 in Fig. 8b) and a saddle point (point 2 in Fig. 8b). Thus, if a cluster hits the wall upstream of point 2, it would eventually stop at point 1. Otherwise, the cluster would slide downstream and escape (represented by the solid trajectory). The positions of points 1 and 2 depend on the strength of the magnetic field and the hydrodynamic drag force on the cluster. The two points move downstream and eventually disappear as m decrease or as d increases. A simple analysis on such points for a bar magnet is given in [24].

In the slip model, all of the clusters which are captured by the magnet stop at the point denoted '1' in Fig. 8b. Thus, it is necessary to ensure that the point '1' lies within the tumor itself. In the following, we

assume the tumor radius $R_{tumor} = 100R = 0.01$ m. This requires a very focused magnetic field, i.e., the dipole model would have a very small d. For example, the magnet with $m = 1,066$ A m^2 and $d = 3.372 \times 10^{-2}$ m is strong enough to attract all the clusters to the vessel wall, but since they impact the wall upstream of the target, the clusters may not arrive at the tumor within a reasonable amount of time. In reality, though, the particles are designed to be small enough to pass through the capillary wall toward the target or may slide along the vessel wall. A simple analysis helps to understand the slow nature of the sliding speed. When the cluster is very close to the wall, the convective velocity is approximately $u \approx (1 - ((R - a)/R)^2)u_{max} = 1.27 \times 10^{-5}$ m s^{-1}. The cluster slides over the tumor radius on a timescale of $\frac{R_{tumor}}{u} \sim 10^3$ s. This estimate would be longer if the magnetic force acts against the sliding motion. An example is the solid trajectory in Fig. 8, which reaches the wall at $t = 5.25$ s but slides to $x = 100R$ at $t = 714$ s. During such a long time interval, a number of events which we have not taken into account may come into play, such as the likely penetration across the endothelium and through the capillary wall toward the target.

One aspect of the slip model which could be improved is that the Stokes drag is no longer valid when the clusters are very close to the vessel wall. Richardson et al. [24] adopted the following drag law in the flow direction:

$$\mathbf{F}_s \cdot \mathbf{e}_x = -6\pi \eta a K_f \left(0.269\dot{x} \ln \left(\frac{a}{\gamma} \right) - a \left. \frac{\partial u}{\partial n} \right|_{\partial \Omega} \right) \quad \gamma \ll R, \tag{29}$$

where $\left. \frac{\partial u}{\partial n} \right|_{\partial \Omega}$ is the normal directional derivative of flow velocity at the vessel wall, γ is the shortest distance between the particle and the wall, and $K_f = 1.858$. In addition to Stokes drag, therefore, this model also considers the extra drag due to the vessel wall and predicts a slower sliding motion. In practice, any roughness of the vessel wall such as plaque would hinder further sliding. Therefore, it is more reasonable to use the no-slip model as a basis for the rest of this paper, i.e., the clusters stay where they are after they hit the vessel wall, keeping in mind the high probability of penetrating the wall and arriving at the target. By 'capture', we shall mean that the impact position at the wall is within the tumor radius. Ideally, the tumor lies on the vessel wall for this treatment.

3.3.3 A guideline for the design of magnets

Let us consider the case $d \gg R_{tumor} \gg R$. The cluster that passes over the tumor along the cylindrical axis experiences the viscous drag

$$f_v = 6\pi \eta a u_{max} \tag{30}$$

in the x-direction and magnetic force

$$f_m = \left(\frac{3\chi}{3 + \chi} \right) \left(\frac{\mu_0}{\pi} \right) \left(\frac{m^2 a^3}{d^7} \right) \tag{31}$$

in the $-z$ direction. In Eq. (30), we have used the fact that the distance between the cluster and the dipole is approximately d. A dimensionless parameter that characterizes the significance of the magnetic force can be constructed from the two above,

$$\Pi = \frac{f_m}{f_v} = \left(\frac{3\chi}{3 + \chi} \right) \left(\frac{\mu_0 a^2}{6\pi^2 \eta v_{max}} \right) \left(\frac{m^2 a^2}{d^7} \right). \tag{32}$$

If the cluster is released from $(-R_{tumor}, 0, 0)$, then it reaches the tumor if and only if

$$\frac{\Delta z}{\Delta x} \geq \frac{R}{2R_{tumor}}, \tag{33}$$

where Δx and Δz are the absolute values of cluster displacements in the x and z directions. As the cluster motion is solely driven by f_m and f_v, it is obvious that $\frac{f_m}{f_v} \approx \frac{\Delta z}{\Delta x}$. Therefore, the above inequality transforms to
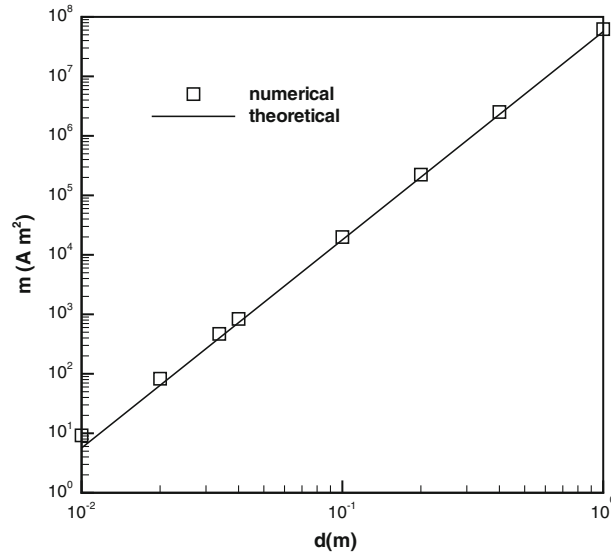
$$\Pi \geq \frac{R}{2R_{tumor}}. \tag{34}$$

Fig. 9 Critical values for m that attract clusters from $(-R_{\text{tumor}}, 0, 0)$ to the tumor versus the distance d. The theoretical curve is from Eq. (34), which agrees well with the numerical values (*open square*). $R = 10^{-4}$ m, $u_{\max} = \frac{2}{\pi} \times 10^{-2}$ m s^{-1}, $a = 10^{-7}$ m, $\eta = 0.004$ Pa s, $\chi = 0.2$, and $R_{\text{tumor}} = 100R$

The case of equality in this equation yields the 'critical' values for the corresponding magnet parameters d and m. These are shown in Fig. 9 for the case $R_{\text{tumor}} = 100R$. For each d, computations are performed to find the critical m, with at least three significant digits of accuracy. The agreement between Eq. (34) and the numerical experiment is excellent. There is only a slight difference when d approaches 0.01 m. At $d = 0.01$ m, the numerical and theoretical values of m are 9.2 and 5.7 A m^2, respectively. The reason is that the assumption $d \gg R$ is no longer valid there. Further, this fact can easily be incorporated by replacing d in Eqs. (31), (32) by an average distance between the cluster and the dipole, $\bar{d}$. If we take $\bar{d} = \sqrt{d^2 + \left(\frac{R_{\text{tumor}}}{2}\right)^2}$, then Eq. (34) yields $m = 8.4$ A m^2, which improves the agreement with the numerical value. In conclusion, Eq. (34) is an effective estimate for $d \gg R_{\text{tumor}} \gg R$.

In practical applications, it is desirable that the magnet attracts all of the clusters to a tumor. For all possible cluster positions, the maximum displacement in the z direction is just the vessel diameter $2R$. Equation (34) is modified accordingly to

$$\Pi \geq \Pi_c = \frac{R}{R_{\text{tumor}}}, \tag{35}$$

giving the condition for the capture of all the clusters released just upstream of the tumor. Considering Eq. (32), the critical values of m and d that start to capture all the clusters satisfy the power-law relationship $m_c \sim d_c^{7/2}$.

This criterion overestimates the effect of viscous drag, which should be smaller than Eq. (30) when the cluster is placed away from the vessel centerline. Thus, Eq. (35) must be a sufficient condition for the capture of all clusters if $d \gg R_{\text{tumor}} \gg R$ is satisfied.

To verify Eq. (35), we introduce the concept of 'capture rate'. We assume that a cluster is equally likely to appear at any specific location at the circular inlet cross-section and take into account the background parabolic velocity profile. Thus, the clusters are initially uniformly distributed within the vessel cross-section, and then, the suspension is forced through the vessel. Since the velocity is higher at the centerline, more particles are carried through along the center of the vessel. Therefore, we define the capture rate to be weighted with the velocity $1 - (\frac{r}{R})^2$. The capture rate of clusters is then given by the probability function

$$p = \frac{\int_0^{2\pi} \int_0^R f(r, \phi)(1 - (r/R)^2) r \, dr \, d\phi}{\int_0^{2\pi} \int_0^R (1 - (r/R)^2) r \, dr \, d\phi}, \tag{36}$$

where (r, ϕ) are the polar coordinates on the $y - z$ plane. $f(r, \phi) = 1$ if the cluster initially at (r, ϕ) hits the tumor, i.e., the final position satisfies $|x| < R_{\text{tumor}}$; otherwise, $f(r, \phi) = 0$. The numerical evaluation is
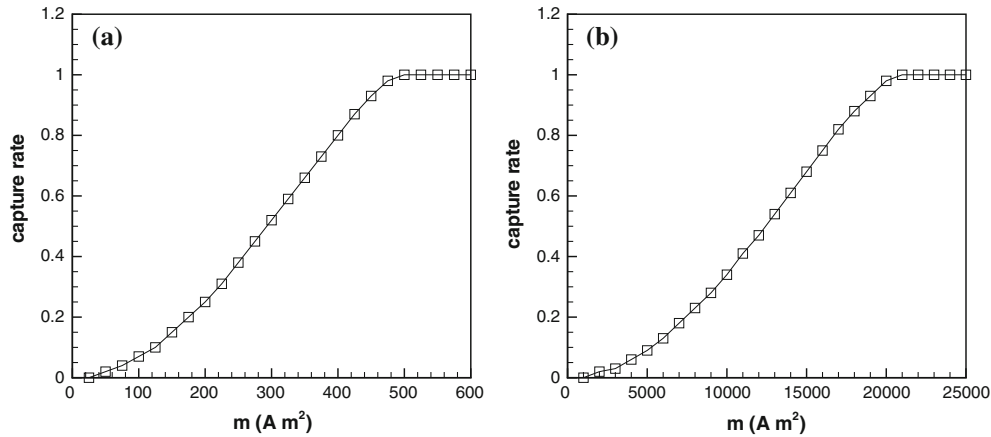
Fig. 10 Capture rate versus dipole moment m with **a** $d = 0.03372$ m and **b** $d = 0.1$ m. $R = 10^{-4}$ m, $u_{max} = \frac{2}{\pi} \times 10^{-2}$ m s^{-1}, $a = 10^{-7}$ m, $\eta = 0.004$ Pa s, $\chi = 0.2$, and $R_{tumor} = 100R$. Clusters are released at $x = -R_{tumor}$

carried out by dividing the circular cross-section into cells with $\Delta r = R/M$ and $\Delta \phi = \pi/N$, where M and N are the number of cells in radial and circumferential direction, respectively. Only half of the cross-section needs to be used, due to symmetry in the y-direction. In the following, we choose $M = N = 50$ which gives numerical accuracy to 3 decimal places.

Figure 10 shows capture rates for a tumor size $R_{tumor} = 100R$. The clusters are initially uniformly distributed across the cross-section before simultaneous release. Each data point in the figure consists of simulations to count the clusters which are captured at the target. We can see that the capture rate achieves 100% around $m_c = 500$ and 2.1×10^4 A m^2 for $d = 0.03372$ and 0.1 m, respectively. Equation (35) predicts $m_c = 5.63 \times 10^2$ and 2.53×10^4 A m^2. Thus, the relative error between the numerical and theoretical values is less than 20%, indicating a reasonable estimate. We see from Fig. 11 that for small magnetic forces the capture rate is quadratic in m for a class of velocity profiles for a power-law fluid, $v = v_{max} \left[1 - \left(\frac{r}{R} \right)^n \right]$, $n = 1, 2, 4, 8$. This velocity profile includes, as an extreme case, a centrally placed plug flow with a linear velocity profile near the walls and is a first approximation for the shear-thinning rheology of blood flow [47]. The fit for the capture rate $p \sim m^\alpha$ for $m \leq 300$ A m^2 yields the exponents $\alpha = 1.88, 1.91, 1.94$, and 1.99 for $n = 1, 2, 4$, and 8. Thus, $p \sim m^2$ is universal for this range of parameters; this has been observed previously, for instance, see the review article of [50]. The velocity profile does affect the capture rate, e.g., the capture rates at $m = 300$ are $p = 0.35, 0.25, 0.19$, and 0.17 for the four velocity profiles. However, the critical m for 100% capture rate is not sensitive to the velocity profile. Note that the $p \sim m^2$ obtained here is consistent with that obtained in [51]. In [51], the 'line capture efficiency η_l' is found to be proportional to the square root of the magnetic force, or m. However, this result is obtained based on a planar flow, linearizing the velocity profile, and without weighting η with the velocity.

In practice, the tumor, blood, and cluster parameters are fixed. Our aim is to design the magnet such that the capture rate is as high as possible. When a superconducting magnet is used, the model parameter d in (27) represents the physical distance from the center of the magnet to the vessel wall. This distance is interpreted as the sum of the distance from the center of the magnet to its surface and from its surface to the vessel wall. Thus, (35) is again used to estimate the critical value m_c. Finally, m_c is transformed back to the relevant superconducting magnet parameters. Note that it is not necessary for the dipole moment to go beyond m_c. If a capture rate lower than 100% is acceptable, the dipole moment m can be slightly lower than m_c. For example, Fig. 10a shows that a capture rate of 10% is still obtained when $m \approx m_c/4$.

In this section, we have assumed a constant susceptibility. On the other hand, the inclusion of a nonlinear dependence of susceptibility on the magnetic field strength is of interest when the applied magnetic field is large and can be incorporated and addressed in future work. In order to perform a preliminary assessment of the effect of a variable susceptibility, the nonlinear Langevin fit for the magnetization versus field strength data is taken from [35]. The susceptibility can be represented as a function of the magnetic field,

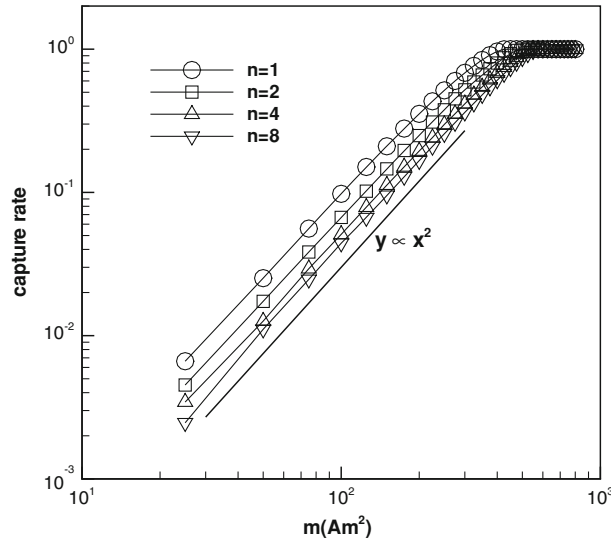$$\chi(H) = \frac{M_s}{H} \left[\coth \left(\frac{H}{H_s} \right) - \frac{H_s}{H} \right],$$

Fig. 11 Capture rate versus dipole moment m for velocity profiles of a class of shear-thinning power-law fluids: $v = v_{\max} \left[1 - \left(\frac{r}{R} \right)^n \right]$, $r = \sqrt{y^2 + z^2}$. n is the index of the power-law. $d = 0.03372$ m, $R = 10^{-4}$ m, $u_{\max} = \frac{2}{\pi} \times 10^{-2}$ m s^{-1}, $a = 10^{-7}$ m, $\eta = 0.004$ Pa s, $\chi = 0.2$, and $R_{\text{tumor}} = 100R$. Clusters are released at $x = -R_{\text{tumor}}$

where $M_s = 2.34 \times 10^4$ and $H_s = 1.52 \times 10^4$ Am^{-1}. To give an idea of the sample values, we mention $\chi = 0.51$ at $H = 10^3$ Am^{-1}, $\chi = 0.20$ at $H = 10^5$ Am^{-1}, and $\chi = 0.02$ at $H = 10^6$ Am^{-1}. Figure 12 shows numerical results for the capture rate versus magnetic moment with $d = 0.03372$ m, vessel of radius $R = 10^{-4}$ m, $u_{\max} = \frac{2}{\pi} \times 10^{-2}$ m s^{-1}, nanoparticle radius $a = 10^{-7}$ m, $\eta = 0.004$ Pa s, and $R_{\text{tumor}} = 100R$. The clusters are released at $x = -R_{\text{tumor}}$. These conditions are identical to those of Fig. 10a except for χ. In comparison with Fig. 10a, the capture rate is much lower than that with the constant χ value of 0.2. This is not surprising because the effective magnetic susceptibility reduces to 0.0012 at $m = 500$ Am^2, due to a large $H \sim 2 \times 10^6$ Am^{-1} at the target. Correspondingly, the magnetic force drops by the factor 18. Considering the fact that the magnetization has reached saturation at this m, the critical magnetic moment needs to be boosted by 18 times to achieve approximately the same magnetic force as with constant χ. This is consistent with the observed $m_c = 8,000$ Am^2, which is required to achieve 100% capture rate. The achievement of magnetic saturation would further affect the scaling arguments of this section. For example, the m^2 factor in the magnetic force in (31) would be reduced to m^1.

3.3.4 Influence of cluster injection location

We have assumed in the previous section that the clusters are uniformly distributed at the plane $x = -R_{\text{tumor}}$ and injected right before the tumor. In this subsection, we generalize this and release the clusters at a variety of locations $x = x_0$.

The influence of x_0 on the capture rate is investigated in more detail by using magnetic parameters that generate capture rates away from both 0 and 100%. Based on Fig. 10a, we choose $d = 0.03372$ m and $m = 300$ A m^2 which yields a capture rate of 0.515 at $x_0 = -100R$. The capture rate for varying x_0 is plotted in Fig. 13. Here, the tumor capture rate refers to the percentage of clusters that hit the tumor, while the wall capture rate refers to the percentage of all clusters that hit the vessel wall. The tumor capture rate achieves its maximum at $x_0 = -R_{\text{tumor}}$, which means it is optimal to inject the drug right before the tumor. The transit time for the cluster to pass over the magnet decreases as the injection location approaches the tumor. As a result, clusters are less affected by the magnet, which leads to a monotonically decreasing wall capture rate.

The distribution of clusters on the vessel wall is shown in Fig. 14. Part (a) of the figure shows a bell-shaped normal distribution centered at $x \approx 0$. The optimal placement of the magnet is therefore directly below the center of the tumor. As x_0 moves toward the tumor, the distribution becomes truncated from the left as shown in Fig. 14b. The standard deviation in (a) is $159R$, which is roughly one half of d. The calculations with different m and d also support this relationship. As the tumor only covers a portion of the width of the distribution, the tumor capture rate is lower than the wall capture rate. To maximize the tumor capture rate, it is preferable to
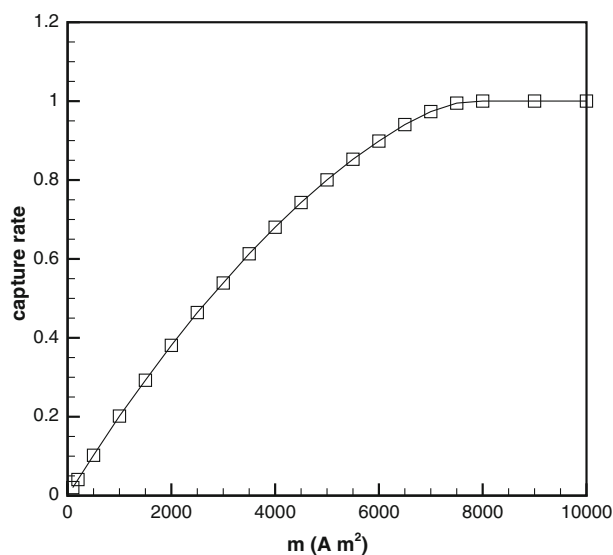
Fig. 12 Capture rate versus magnetic moment for magnetic susceptibility χ which varies according to a Langevin fit to the magnetization data of [35]. $d = 0.03372$ m, vessel of radius $R = 10^{-4}$ m, $u_{max} = \frac{2}{\pi} \times 10^{-2}$ ms^{-1}, nanoparticle radius $a = 10^{-7}$ m, $\eta = 0.004$ Pa s, and $R_{tumor} = 100R$. The clusters are released at $x = -R_{tumor}$. These conditions are the same as those of Fig. 10a except for χ, which varies in this figure
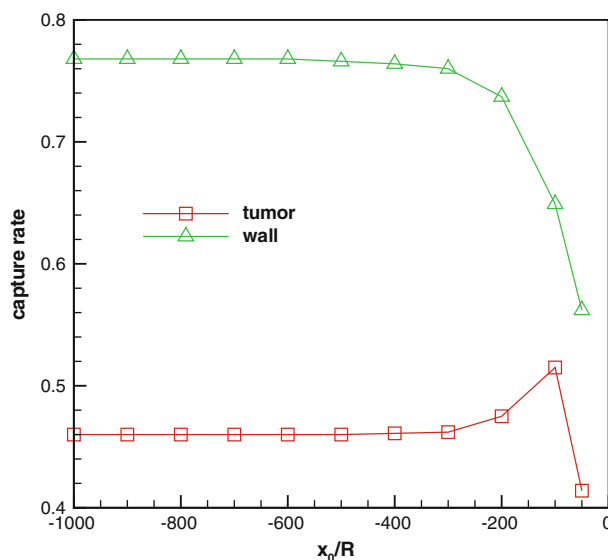
Fig. 13 Capture rates as a function of cluster initial position x_0. $R = 10^{-4}$ m, $u_{max} = \frac{2}{\pi} \times 10^{-2}$ ms^{-1}, $a = 10^{-7}$ m, $\eta = 0.004$ Pa s, $\chi = 0.2$, $R_{tumor} = 100R$, $d = 0.03372$ m, and $m = 300$ Am^2

have a tumor size that is comparable with d. In other words, the magnet size should match the tumor size if the former is not strong enough to attract all of the clusters to tumor.

3.4 Brownian motion

Brownian motion affects the cluster trajectory and may even cause the cluster to hit or miss the tumor. Figure 15 shows the effect of Brownian motion for the larger cluster size $a = 10^{-7}$ m. For each stochastic trajectory, the simulation stops once the trajectory intersects the wall of the blood vessel. The Brownian motion is visible, but not to the extent that significantly influences the capture rate.
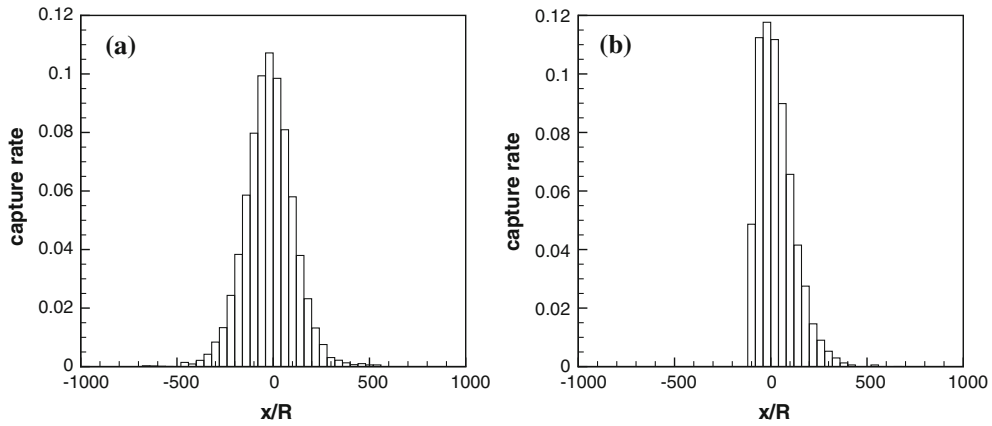
Fig. 14 Distribution of clusters that hit the vessel wall. **a** $x_0 = -1000R$ and **b** $x_0 = -100R$. The height of each bar represents the cluster capture rate by the x range covered by that bar. $R = 10^{-4}$ m, $u_{max} = \frac{2}{\pi} \times 10^{-2}$ m s^{-1}, $a = 10^{-7}$ m, $\eta = 0.004$ Pa s, $\chi = 0.2$, and $R_{tumor} = 100R$

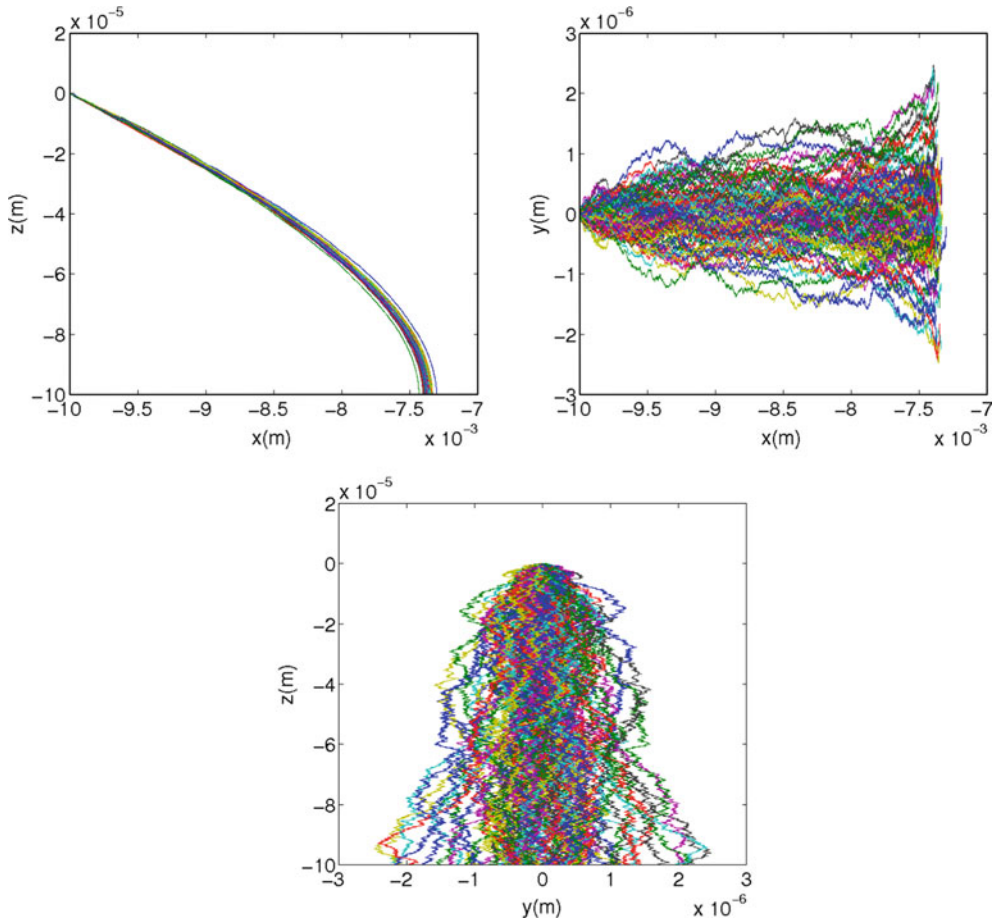**Fig. 15** Cluster trajectories in the $x - z$ plane with $y = 0$, $x - y$ plane with $z = 0$ and $y - z$ plane with $x = 0$. Radius of a cluster $a = 10^{-7}$ m (relatively large). The simulations include the effect of Brownian motion. $R = 10^{-4}$ m, u_{max} in (1) is $\frac{2}{\pi} \times 10^{-2}$ m s^{-1}, $\eta = 0.004$ Pa s, $\chi = 0.2$, $m = 1056$ Am^2, $d = 0.03372$ m, and time step $\Delta t = 2 \times 10^{-4}$ s. The clusters are released from $(-100R, 0, 0)$. 100 stochastic trajectories are shown
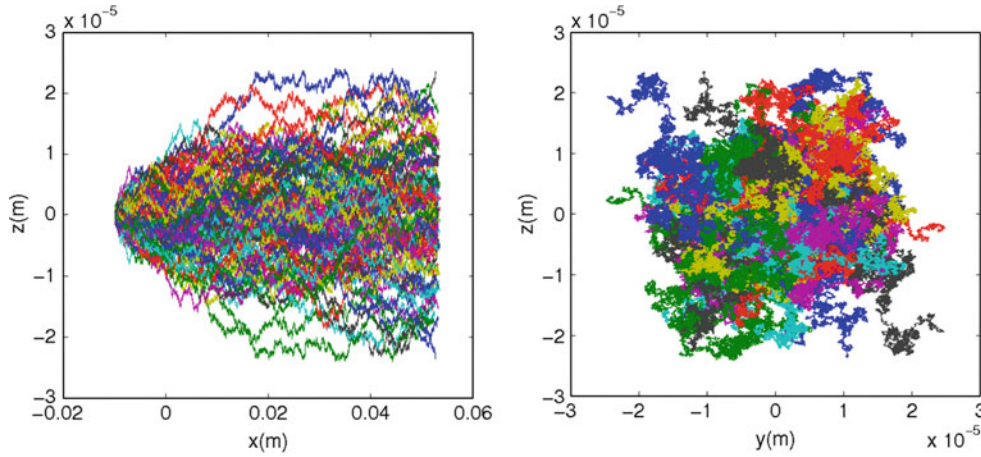
Fig. 16 Cluster trajectories with Brownian motion for smaller clusters. $a = 10^{-8}$ m. Other parameters are the same as in Fig. 15. The simulations are performed to $t = 10$ s

Due to Brownian motion, the cluster position has a standard deviation (square root of the variance)

$$\delta = \sqrt{\frac{2k_B T}{6\pi \eta a} t}, \tag{37}$$

in any direction over time t. Let us take the trajectories of Fig. 15 for example. Based on Fig. 7, the time duration of the trajectories is approximately $t = 0.59$ s. Equation (37) predicts $\delta = 8 \times 10^{-7}$ m. For a normal distribution, three standard deviations cover 99.7% of the distribution. This is consistent with the width of the trajectories in Fig. 15b, c. As $\delta \ll R$, we conclude that the Brownian motion can be safely neglected for the these parameters.

Brownian motion becomes important when the cluster size decreases, which is expected, and shown in Fig. 16. The simulations end at $t = 10$ s. Equation (37) predicts $\delta = 1.07 \times 10^{-5}$ m for $a = 10^{-8}$ m, which again agrees with the boundary of trajectories in Fig. 16. For $a = 10^{-8}$ m, the simulation without the Brownian motion is simply a straight line parallel to the x-axis. Brownian motion for this cluster size is still not large enough to bring the cluster to the vessel wall. As the cluster size is further reduced, the Brownian motion becomes so dominant that some trajectories hit the vessel wall. The analysis above is supported by the left part of the solid curve in Fig. 17. For clusters of size $a < 10^{-9}$ m, some trajectories hit the wall due to the strong Brownian motion. As a increases, Brownian motion decreases, and therefore the capture rate drops. For clusters of size $a > 2 \times 10^{-8}$ m, the magnetic force is strong enough to attract some trajectories to the tumor. This reveals two different mechanisms for cluster capture: magnetic force for the large clusters and Brownian motion for the small clusters.

Brownian motion is also more significant for the clusters that are initially closer to the vessel wall, as verified in Fig. 17 by the higher capture rates for small clusters that are closer to wall. If the cluster is released from $(-R_{\text{tumor}}, 0, z_0)$ and the local convection velocity is $U = (1 - (z_0/R)^2)u_{\text{max}}$, then the time that the cluster passes over the tumor ($x \in (-R_{\text{tumor}}, R_{\text{tumor}})$) is approximately $t = 2R_{\text{tumor}}/U$. Meanwhile, the Brownian motion starts to affect the capture of a cluster when $3\delta \gtrsim R - |z_0|$. The equality gives the cluster sizes $a = 3.2 \times 10^{-10}$, 1.7×10^{-9} and 1.7×10^{-7} m for $z_0 = 0$, $-0.5R$ and $-0.9R$, respectively. The first two values of a are very close to the numerical values (about 6×10^{-10} and 3×10^{-9} m) at which the capture rate decreases to zero. However, for $z_0 = -0.9R$, there is a large discrepancy. The reason lies in the fact that the effect of Brownian motion weakens when it competes with magnetic force. For $z_0 = -0.9R$, the effect of the magnetic force is so strong that the capture rate remains 100% until $a \approx 10^{-8}$ m, which is much smaller than the value predicted by δ.

In summary, the effect of Brownian motion is limited for the more traditional cluster sizes. Those that are smaller than 10^{-8} m or very close to the vessel wall are significantly affected. The latter would apply to a small fraction of all the clusters. In particular, for the parabolic velocity profile, the percentage of clusters within $\sqrt{y^2 + z^2} \le z_0$ is calculated to be
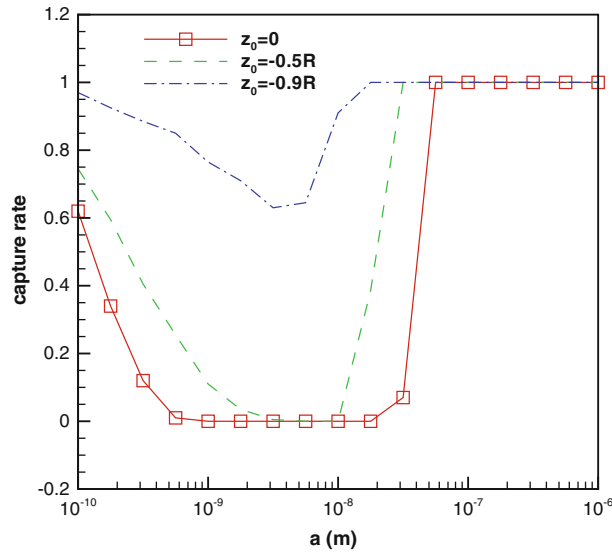
Fig. 17 Capture rate as a function of cluster radius. Clusters are injected at $(-100R, 0, z_0)$ for $z_0 = 0, -0.5R, -0.9R$. The effects of Brownian motion are included. $R_{\text{tumor}} = 100R$. Each data point is obtained based on 200 stochastic trajectories with time step $\Delta t = 2 \times 10^{-4}$ s

$$p = 2(z_0/R)^2 - (z_0/R)^4. \tag{38}$$

Thus, the clusters with initial positions satisfying $\sqrt{y^2 + z^2} > 0.9R$ comprise just 3.6% of the total amount.

4 Conclusions

We study the motion of spherical superparamagnetic clusters of roughly 10^{-7} m carried in a flow through a channel of radius 10^{-4} m, guided by a magnetic field. The governing equations are integrated numerically to obtain paths of motion and capture rates. Theoretical analyses are performed and supported by the numerical simulations. The effect of Brownian motion is also studied for the smallest clusters. The investigation of agglomeration [52,53] is left for future work, as is the interaction of the clusters with red blood cells. Our model for flow through small venules warrants comparisons with experimental data, but the authors are not aware of controlled experiments with well-characterized flow conditions on the class of superparamagnetic nanoparticle clusters which are recently being developed [54]. The major results can be summarized as follows:

(i) A point dipole is used to model an external magnet. While this approximation is correct when the magnet is small compared with the distance from the particle, and significantly simplifies the analytical and numerical solutions to the forces acting on the particles, we mention the limits of validity of this approximation. In order to model a bar magnet which is not small, an improved approximation is to use a continuous distribution of point dipoles over the magnet volume. At the other extreme, the need for a high magnetic field gradient leads to the use of a superconducting coils system. In our parameter range, we verified with Fig. 5 that the analytical dipole formula (27) is a very good approximation. An improved model would essentially be the Biot-Savart law, with inputed data on the physical shape of the coils in the superconducting magnet, its radius, the number of times it winds, and the applied current. To derive the analytical formula for the field strength, Maxwell's equations are used: the magnetic field $\mathbf{H}$, the current density $\mathbf{J}$, and a magnetic vector potential $\mathbf{A}$ are related by $\nabla \cdot \mathbf{H} = 0$, $\nabla \times \mathbf{H} = \mathbf{J}$, $\mathbf{H} = \nabla \times \mathbf{A}$, $\nabla \cdot \mathbf{A} = 0$. This yields a Laplacian, $\text{curl}(\text{curl } \mathbf{A}) = -\Delta \mathbf{A} = \mathbf{J}$, which is solved using the known Green's functions for the Laplacian operator. Thus, $\mathbf{A}$ is calculated by evaluating a number of integrals. From this, $\mathbf{H}$ is calculated and fed back as $\mathbf{H}_e$ into the force equation (6).

(ii) The sliding motion of the clusters on the vessel wall occurs on a slow timescale. As a result, we may assume that a cluster remains at the point of impact with the vessel wall.

(iii) Optimal treatment conditions for a tumor require that the magnet be placed beneath the center of the tumor and the clusters be injected into the bloodstream just before the tumor.

(iv) Equation (35) gives a useful estimate for the critical values of the magnet parameters m and d, which ensure that the tumor capture rate is 100%.

(v) The capture rate scales with the square of dipole moment for a variety of velocity profiles relevant to blood flow, such as the shear-thinning power-law fluid. Hence, the capture rate shows limited sensitivity to changes in the velocity profile.

(vi) In the case that the magnet parameters are not sufficiently strong to achieve a 100% capture rate, we find that the clusters deposited on the vessel wall follow a normal distribution. The standard deviation is approximately half of the distance d between the magnetic dipole and the blood vessel. To optimize the capture rate, the distance d should match the tumor size.

(vii) Brownian motion has a significant influence on cluster paths for radii much less than $a = 10^{-7}$ m.

References

1. Alexiou, C., Arnold, W., Klein, R.J., Parak, F.G., Hulin, P., Bergemann, C., Erhardt, W., Wagenpfeil, S., Lübbe, A.S.: Loco-regional cancer treatment with magnetic drug targeting. Cancer Res. **60**, 6641–6648 (2000)
2. Voltairas, P.A., Fotiadis, D.I., Massalas, L.K.: Elastic stability of silicone ferrofluid internal tamponade (sfit) in retinal detachment surgery. J. Magn. Magn. Mater. **225**, 248–255 (2001)
3. Voltairas, P.A., Fotiadis, D.I., Michalis, L.K.: Hydrodynamics of magnetic drug targeting. J. Biomech. **35**, 813–821 (2002)
4. Pankhurst, Q.A., Connolly, J., Jones, S.K., Dobson, J.: Applications of magnetic nanoparticles in biomedicine. J. Phys. D **36**, 167–181 (2003)
5. Neuberger, T., Schopf, B., Hofmann, H., Hofmann, M., von Rechenberg, B.: Superparamagnetic nanoparticles for biomedical applications: possibilities and limitations of a new drug delivery system. J. Magn. Magn. Mater. **293**, 483–496 (2005)
6. Buzea, C., Pacheco, I.I., Robbie, K.: Nanomaterials and nanoparticles: sources and toxicity. Biointerphases **2**, MR17–MR71 (2007)
7. Chertok, B., Moffat, B.A., David, A.E., Yu, F., Bergemann, C., Ross, B.D., Yang, V.C.: Iron oxide nanoparticles as a drug delivery vehicle for MRI monitored magnetic targeting of brain tumors. Biomaterials **29**, 487–496 (2008)
8. Roca, A.G., Costo, R., Rebolledo, A.F., Veintemillas-Verdaguer, S., Tartaj, P., González-Carreno, T., Morales, M.P., Serna, C.J.: Progress in the preparation of magnetic nanoparticles for applications in biomedicine. J. Phys. D: Appl. Phys. **42**, 224002 (2009)
9. Berry, C.C.: Progress in functionalization of magnetic nanoparticles for applications in biomedicine. J. Phys. D: Appl. Phys. **42**, 224003 (2009)
10. Pankhurst, Q.A., Thanh, N.K.T., Jones, S.K., Dobson, J.: Progress in applications of magnetic nanoparticles in biomedicine. J. Phys. D: Appl. Phys. **42**, 224001 (2009)
11. Mishra, B., Patel, B.B., Tiwari, S.: Colloidal nanocarriers: a review on formulation technology, types and applications toward targeted drug delivery. Nanomed. Nanotechnol. Biol. Med. **6**, 9–24 (2010)
12. Shapiro, B.: Toward dynamic control of magnetic fields to focus magnetic carriers to targets deep inside the body. J. Magn. Magn. Res. **321**, 1594–1599 (2009)
13. Takeda, S., Mishima, F., Fujimoto, S., Izumi, Y., Nishijima, S.: Development of magnetically targeted drug delivery system using superconducting magnet. J. Magn. Magn. Mater. **311**, 367–371 (2007)
14. Rosensweig, R.E.: Ferrohydrodynamics. Cambridge University Press, New York (1985)
15. Qiao, X., Bai, M., Tao, K., Gong, X., Gu, R., Watanabe, H., Sun, K., Wu, J., Kang, X.: Magnetorheological behavior of polyethylene glycol-coated fe_3o_4 ferrofluids. J. Soc. Rheol. Jpn. **38**, 23–30 (2010)
16. Thompson Mefford, O., Carroll, M.R.J., Vadala, M.L., Goff, J.D., Mejia-Ariza, R., Saunders, M., Woodward, R.C., St. Pierre, T.G., Davis, R.M., Riffle, J.S.: Size analysis of PDMS-magnetite nanoparticle complexes: experiment and theory. Chem. Mater. **20**, 2184–2191 (2008)
17. Mefford, O.T., Vadala, M.L., Carroll, M.R.J., Mejia-Ariza, R., Caba, B.L., St. Pierre, T.G., Woodward, R.C., Davis, R.M., Riffle, J.S.: Stability of polydimethylsiloxane-magnetite nanoparticles against flocculation: Interparticle interactions of polydisperse materials. Langmuir **24**, 5060–5069 (2008)
18. Miles, W.C., Goff, J.D., Huffstetler, P.P., Mefford, O.T., Riffle, J.S., Davis, R.M.: The design of well-defined PDMS-magnetite complexes. Polymer **51**, 482–491 (2010)
19. Balasubramaniam, S., Pothayee, N., Lin, Y., House, M., Woodward, R.C., St. Pierre, T.G., Davis, R.M., Riffle, J.S.: Poly(N-isopropylacrylamide)-coated superparamagnetic iron oxide nanoparticles: relaxometric and fluorescence behavior correlate to temperature-dependent aggregation. Chem. Mater. **23**, 3348–3356 (2011)

20. Pothayee, N., Balasubramaniam, S., Davis, R.M., Riffle, J.S., Carroll, M.R.J., Woodward, R.C., St. Pierre, T.G.: Synthesis of ready-to-absorb polymeric nanoshells for magnetic iron oxide nanoparticles via atom transfer radical polymerization. Polymer **52**, 1356–1366 (2011)
21. Mejia-Ariza, R., Celebi, O., Riffle, J.S., Davis, R.M.: Formation of magnetite-containing nanoparticles using a multi-inlet vortex mixer. AIChE Annual Meeting (2008)
22. Ganguly, R., Zellmer, B., Puri, I.K.: Field-induced self-assembled ferrofluid aggregation in pulsatile flow. Phys. Fluids **17**, 097104 (2005)
23. Barrera, C., Herrera, A., Zayas, Y., Rinaldi, C.: Surface modification of magnetite nanoparticles for biomedical applications. J. Magn. Magn. Mater. **321**, 1397–1399 (2009)
24. Richardson, G., Cummings, L., King, J., Gaffney, E., Hazelwood, L., Chapman, J.: Drug delivery by magnetic microspheres. In: Report on a Problem Studied at the UK Mathematics-in-Medicine Study Group Nottingham 2000, http://www.maths-in-medicine.org/uk/2000/drug-delivery (2001)
25. Grief, A.D., Richardson, G.: Mathematical modelling of magnetically targeted drug delivery. J. Magn. Magn. Mater. **293**, 455–463 (2005)
26. Dobson, J.: Magnetic nanoparticles for drug delivery. Drug Dev. Res. **67**, 55–60 (2006)
27. Nacev, A., Beni, C., Bruno, O., Shapiro, B.: Magnetic nanoparticle transport within flowing blood and into surrounding tissue. Nanomedicine **5**, 1459–1466 (2010)
28. Nacev, A., Beni, C., Bruno, O., Shapiro, B.: The behaviors of ferromagnetic nano-particles in and around blood vessels under applied magnetic fields. J. Magn. Magn. Mater. **323**, 651–668 (2011)
29. Mishima, F., Takeda, S., Izumi, Y., Nishijima, S.: Three dimensional motion control system of ferromagnetic particles for magnetically targeted drug delivery systems. IEEE Trans. Appl. Superconduct. **16**, 1539–1542 (2006)
30. Haverkort, J.W., Kenjeres, S., Kleijn, C.R.: Computational simulations of magnetic particle capture in arterial flows. Ann. Biomed. Eng. **37**, 2436–2448 (2009)
31. Darton, N.J., Hallmark, B., Agrawal, P., James, T., Ho, V.H.B., Slater, N.K.H.: On the magnetic field architecture required to capture superparamagnetic nanoparticles in a microcapillary flow. J. Nanopart. Res. **12**, 307–317 (2010)
32. Strauss, D.: Magnetic drug targeting (2007). http://www.comsol.com/showroom/gallery/197
33. Trenado, C., Strauss, D.J.: Magnetic nanoparticles for in vivo applications: a numerical modeling study. In: Deutsch, A., Brusch, L., Byrne, H., de Vries, G., Herzel, H. (eds.) Mathematical Modeling of Biological Systems, Volume I Modeling and Simulation in Science, Engineering and Technology. pages Part IV, 275–280. Birkhäuser Boston, (2007). There are errors, e.g., on p. 277, the correct equation for line 1 is $\mathbf{B} = \mu\mathbf{H} = \mu_0(\mathbf{H} + \mathbf{M})$. On the same page, line 3 should be $\mathbf{B} = \nabla \times \mathbf{A}$ and $\nabla \cdot \mathbf{A} = 0$ which is stated backward. This error is repeated further on. However, the equation which follows uses the correct $\mathbf{B} = \nabla \times \mathbf{A}$. There is an error in the expression for γ, which should equal $(-M_y, M_x)$, and applied to a linear medium in 2D, this should be proportional to $(\partial A/\partial x, \partial A/\partial y)$, showing a sign error in the second component. The arctan expression is an attempt to implement a nonlinear constitutive law. However, such a nonlinear law has the form $\mathbf{M} = f(|\mathbf{H}|)\mathbf{H}$, and clearly the nonlinear function cannot be applied component-wise. These issues are not explained in this paper.
34. LifeForce Hospitals Webserver medmail@usa.net. http://chemo.net/newpage91.htm, Copyright (1999)
35. Afkhami, S., Renardy, Y., Renardy, M., Riffle, J.S., St. Pierre, T.G.: Field-induced motion of ferrofluid droplets through immiscible viscous media. J. Fluid Mech. **610**, 363–380 (2008)
36. Afkhami S., Renardy Y., Renardy M., Riffle J.S., St. Pierre T.G. (2008) Numerical modeling of ferrofluid droplets in magnetic fields. In: Proceedings of XVth International Congress on Rheology. American Institute of Physics (2008)
37. Afkhami, S., Tyler, A.J., Renardy, Y., Renardy, M., Woodward, R.C., St. Pierre, T.G., Riffle, J.S.: Deformation of a hydrophobic ferrofluid droplet suspended in a viscous medium under uniform magnetic fields. J. Fluid Mech. **663**, 358–384 (2010)
38. Chiou, E.P.Y.: Optical tweezers and magnetic tweezers (2007). http://www.seas.ucla.edu/~pychiou/Lecture-14-3 Optical Tweezers and Magnetic Tweezers.pdf, MAE M 282
39. Mikkelsen, C.I.: Magnetic separation and hydrodynamic interactions in microfluidic systems. PhD thesis, Technical University of Denmark (2005)
40. http://www.mathworks.com. Function ode45
41. Cohen, E.G.D., van Zon, R.: Stationary state fluction theorems for driven Langevin systems. Comptes Rendus Physique **8**, 507–517 (2007)
42. Higham, D.J.: An algorithmic introduction to numerical simulation of stochastic differential equations. SIAM Review **43**, 525–546 (2001)
43. Picchini, U.: SDE Toolbox: simulation and estimation of stochastic differential equations with Matlab (2009). http://sdetoolbox.sourceforge.net/
44. Mefford, O.T., Woodward, R.C., Goff, J.D., Vadala, T.P., St. Pierre, T.G., Dailey, J.P., Riffle, J.S.: Field-induced motion of ferrofluids through immiscible viscous media: Testbed for restorative treatment of retinal detachment. J. Magn. Magn. Mater. **311**, 347–353 (2007)
45. House, S.D., Johnson, P.C.: Diameter and blood flow of skeletal muscle venules during local flow regularization. Am. J. Physiol. Heart Circ. Physiol. **250**, H828–H837 (1986)
46. Shaw, S., Murthy, P.V.S.N., Pradhan, S.C.: Effect of non-Newtonian characteristics of blood on magnetic targeting in the impermeable micro-vessel. J. Magn. Magn. Mater. **322**, 1037–1043 (2010)
47. Mukundakrishnan, K., Eckmann, D.M., Ayyaswamy, P.S.: Bubble motion through a generalized power-law fluid flowing in a vertical tube. Ann. NY Acad. Sci. **1161**, 256–267 (2009)
48. Glowinski, R., Pan, T.W., Hesla, T.I., Joseph, D.D., Périaux, J.: A fictitious domain approach to the direct numerical simulation of incompressible viscous flow past moving rigid bodies: application to particulate flow. J. Comput. Phys. **169**, 363–426 (2001)
49. http://www.mathworks.com. Function ode15s
50. Ganguly, R., Puri, I.K.: Microfluidic transport in magnetic MEMS and bioMEMS. Wiley Interdiscip. Rev. Nanomed. Nanobiotechnol. **2**, 382–399 (2010)
51. Haverkort, J.W., Kenjeres, S., Kleijn, C.R.: Magnetic particle motion in a Poiseuille flow. Phys. Rev. E **80**, 016302 (2009)

52. Climent, E., Maxey, M.R., Karniadakis, G.E.: Dynamics of self-assembled chaining in magnetorheological fluids. Langmuir **20**, 507–513 (2004)
53. Zhu, Y., Umehara, N., Ido, Y., Sato, A.: Computer simulation of structures and distributions of particles in MAGIC fluid. J. Magn. Magn. Mater. **302**, 96–104 (2006)
54. Mejia-Ariza, R.: Design, synthesis and characterization of magnetite clusters using a multi inlet vortex mixer. Master's thesis, Virginia Tech (2010)